Article

Cell Systems

Microbial Interaction Network Inference in Microfluidic Droplets

Graphical Abstract

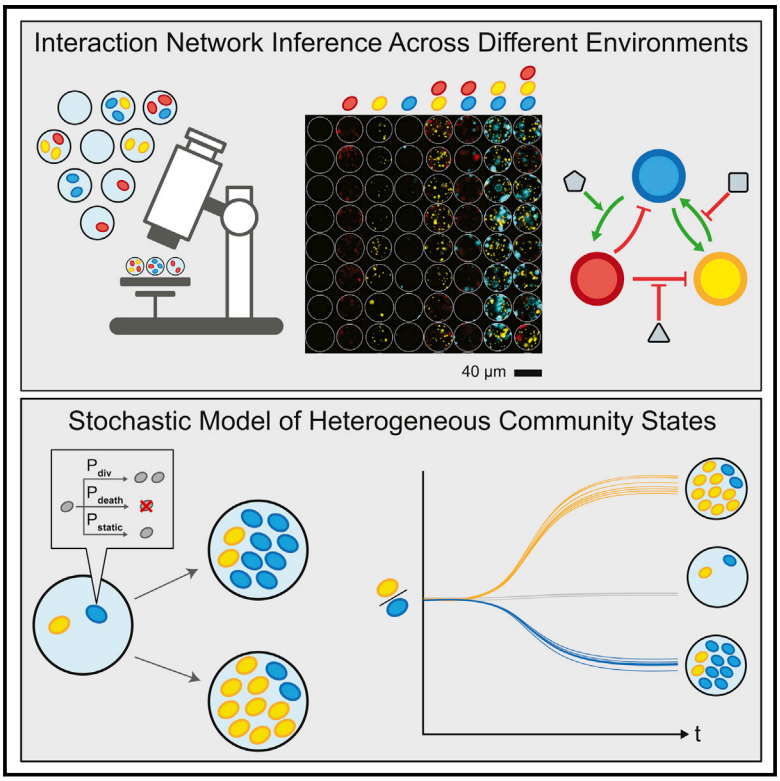

Highlights

- Inference of microbial interaction networks in microfluidic droplets
- Insight into synthetic microbial communities across different environments
- Stochastic model of community assembly to study variability in community states
- Elucidation of a complex web of interactions between antibiotics and a consortium

Authors

Ryan H. Hsu, Ryan L. Clark, Jin Wen Tan, John C. Ahn, Sonali Gupta, Philip A. Romero, Ophelia S. Venturelli

Correspondence

venturelli@wisc.edu

In Brief

Microorganisms often live in complex multi-species communities, where individual members interact with each other and the environment. These interactions are challenging to decipher and dictate the composition, functions, and dynamics of microbial ecosystems. We developed Microbial Interaction Network Inference in microdroplets (MINI-Drop) to identify the interactions within microbial communities across different environments with hundreds to thousands of droplet replicates. We showed that MINI-Drop can identify pairwise and higher-order interactions in a synthetic microbial community and developed a mathematical model to investigate heterogeneity in community assembly in small populations. Finally, we used MINI-Drop to elucidate a complex interaction network between combinations of antibiotics and species in a synthetic microbial community.

Hsu et al., 2019, Cell Systems 9, 1–14
September 25, 2019
https://doi.org/10.1016/j.cels.2019.06.008

CellPress

Please cite this article in press as: Hsu et al., Microbial Interaction Network Inference in Microfluidic Droplets, Cell Systems (2019), https://doi.org/10.1016/j.cels.2019.06.008

Microbial Interaction Network Inference in Microfluidic Droplets

Ryan H. Hsu,[1,4] Ryan L. Clark,[1,4] Jin Wen Tan,[1] John C. Ahn,[1] Sonali Gupta,[1] Philip A. Romero,[1,3] and Ophelia S. Venturelli[1,2,3,5,*]
[1]Department of Biochemistry, University of Wisconsin-Madison, Madison, WI 53706, USA
[2]Department of Bacteriology, University of Wisconsin-Madison, Madison, WI 53706, USA
[3]Department of Chemical & Biological Engineering, University of Wisconsin-Madison, Madison, WI 53706, USA
[4]These authors contributed equally
[5]Lead contact
*Correspondence: venturelli@wisc.edu
https://doi.org/10.1016/j.cels.2019.06.008

SUMMARY

Microbial interactions are major drivers of microbial community dynamics and functions but remain challenging to identify because of limitations in parallel culturing and absolute abundance quantification of community members across environments and replicates. To this end, we developed Microbial Interaction Network Inference in microdroplets (MINI-Drop). Fluorescence microscopy coupled to computer vision techniques were used to rapidly determine the absolute abundance of each strain in hundreds to thousands of droplets per condition. We showed that MINI-Drop could accurately infer pairwise and higher-order interactions in synthetic consortia. We developed a stochastic model of community assembly to provide insight into the heterogeneity in community states across droplets. Finally, we elucidated the complex web of interactions linking antibiotics and different species in a synthetic consortium. In sum, we demonstrated a robust and generalizable method to infer microbial interaction networks by random encapsulation of sub-communities into microfluidic droplets.

INTRODUCTION

Microbial communities have a tremendous impact on diverse environments ranging from the human body to the plant rhizosphere (Berendsen et al., 2012; Clemente et al., 2012). Microbe-microbe and environment-microbe interactions are major determinants of microbial communities and microbiomes (Cao et al., 2019; Venturelli et al., 2016). Deciphering interaction networks in high-dimensional microbial communities is challenging because of the need to rapidly and accurately determine the absolute abundance of each community member across many sub-communities and environments (Cao et al., 2017; Harcombe et al., 2016).

The population sizes of microbial consortia can range from less than ten cells in mixed species biofilm aggregates to 10^{11} cells mL^{-1} in the human colon (Connell et al., 2014; Sender et al., 2016; Stoodley et al., 2001). Cellular growth history, the temporal order of strain colonization, or the initial phase of microbial competition can impact community assembly and lead to significant heterogeneity in community behaviors (von Bronk et al., 2017; Kong et al., 2018; Vega and Gore, 2017; Venturelli et al., 2018; Zhou et al., 2013). Our understanding of microbial consortia in small populations is limited because of technical challenges in the manipulation and analysis of small populations of cells (Connell et al., 2014). Therefore, high-throughput methods that can rapidly resolve microbial interaction networks across different initial community states, population sizes, and environments would enable a better understanding of the key parameters shaping the structure and functions of microbial communities.

Microbial interaction network inference requires accurate measurements of the absolute abundance of each member of the community (Cao et al., 2017; Fisher and Mehta, 2014). Recent experimental efforts have used models trained on measurements of 1–3 member communities to predict community composition or function of up to 12 members to varying degrees of accuracy (Friedman et al., 2017; Guo and Boedicker, 2016; Kong et al., 2018; Mounier et al., 2008; Venturelli et al., 2018). Absolute abundance quantification of each member of a microbial community has ranged from low-throughput selective plating to count colony forming units (tens of samples per experiment) (Mounier et al., 2008) to optical density multiplied by relative abundance based on next-generation sequencing of samples generated through robotic high-throughput culturing (hundreds of samples per experiment) (Venturelli et al., 2018).

Encapsulation of microbial communities into microdroplets has been used to study ecological and evolutionary processes in microbial communities (Bachmann et al., 2013; Park et al., 2011). Water-in-oil droplets can be generated at kilohertz (kHz) rates using microfluidics, wherein cells from a mixed culture are randomly encapsulated into droplets yielding distinct sub-communities that can be studied in parallel (millions of samples per experiment). Each droplet is a miniaturized compartment that can be used to study interactions between community members in small populations. Microfluidic technologies enable the generation of well-controlled droplet environments of ~1% size variation (Guo et al., 2012). However, previous studies have not fully leveraged the capabilities of this technology to quantitatively investigate microbial communities. Further, we lack a systematic method to rapidly infer microbial interactions using droplet microfluidics in different environmental contexts.

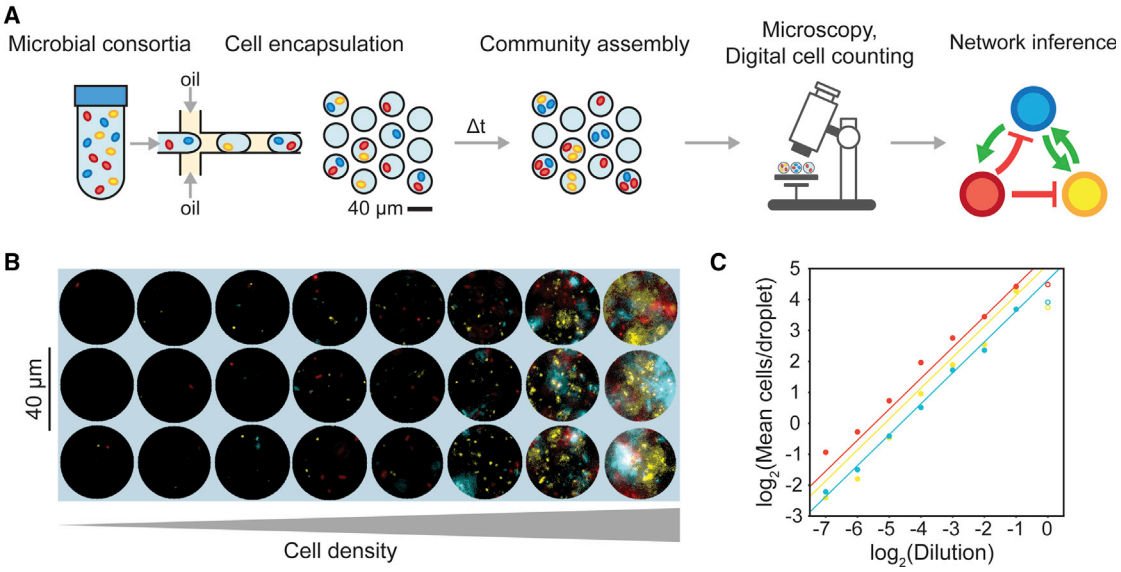

Figure 1. Overview and Characterization of Microbial Interaction Network Inference in Microdroplets (MINI-Drop)

(A) Overview schematic of the MINI-Drop method. A mixed microbial culture and oil are loaded into a droplet-forming microfluidic device. Cells are randomly encapsulated into droplets based on a Poisson distribution. The droplets are incubated for a period of time to allow cell growth and division and then imaged using fluorescent microscopy. A computer vision workflow rapidly identifies droplets and determines the number of each fluorescently labeled strain within each droplet (Figure S1). A microbial interaction network is inferred based on the difference in the mean number of cells in the absence and presence of a partner strain.

(B) Representative fluorescent microscopy images of droplets containing three bacterial strains labeled with YFP (ST Lac*), RFP (EC WT), or CFP (EC Met-) (see Tables S9 and S10).

(C) Scatter plot of the dilution factor of the mixed culture versus the $\log_2$ transform of the mean number of cells per drop (cell count distribution shown in Figure S2A and analysis of mean fluorescence in Figure S2B). Each data point represents the mean of 400–600 droplets and lines denote linear regression fits to the data excluding the highest dilution factor (indicated by empty circles to emphasize divergence from the linear trend). Red, yellow, and blue data points correspond to EC WT, ST Lac*, and EC Met-, respectively.

To address this challenge, we developed Microbial Interaction Network Inference in microdroplets (MINI-Drop). To infer microbial interactions based on the absolute abundance of each strain across hundreds to thousands of samples, we developed an automated computational method coupled to fluorescence microscopy to rapidly segment droplet images and accurately count fluorescently labeled cells within each droplet. We tested the capability of MINI-Drop to infer microbial interactions using a microbial interaction toolbox composed of positive and negative interactions mediated by distinct molecular mechanisms. Our results demonstrate that MINI-Drop can decipher pairwise as well as higher-order interactions by analyzing droplets containing 1–3 strains. We investigated how the molecular composition of the environment shapes the ecological network of a three-member consortium. A probabilistic model of cell growth modified by microbial interactions described the compositional heterogeneity in community states across droplets, providing insight into the forces shaping community assembly in small populations. Finally, we investigated the complex interplay between combinations of antibiotics and temperature on the assembly and species interactions in a three-member consortium.

RESULTS

Microbial interactions represent the net impact (positive, negative, or negligible) of an organism on the growth of another over a specified time interval (Cao et al., 2019). Microbial interactions can be quantified by evaluating the difference in phenotype (e.g., growth response or metabolic activity) of an organism in the absence and presence of another strain (partner strain). Encapsulation of cells in a microbial community into droplets using techniques from droplet microfluidics enables parallel culturing of many sub-communities (Figure 1A). To infer microbial interactions we needed a scalable method to determine the absolute abundance of each strain within each droplet. The average fluorescence in each droplet may not be proportional to the number of cells because of variability in cellular growth rates, which dictates the rate of dilution of the fluorescent reporter (Figure S1A). In addition, absolute abundance information is critical for accurate parameter estimation for computational models (Cao et al., 2017; Fisher and Mehta, 2014). Therefore, we developed an automated procedure using techniques from computer vision to rapidly identify droplets (Figure S1B) and count the number of fluorescently labeled cells in each droplet (Figure S1C). The droplets were binned according to strain composition (Figure S1D) and the cell counts were used to infer the interaction type (positive, negative, or negligible), strength, and directionality (see STAR Methods).

To evaluate the accuracy and dynamic range of the cell counting method, CFP-labeled *E. coli*, RFP-labeled *E. coli*, and YFP-labeled *S. typhimurium* were mixed in equal volumetric ratios and serially diluted to generate a broad range of cell densities (Figure 1B). Each dilution of the mixed culture was encapsulated into 34 picoliter (pL) droplets (40-μm diameter), imaged using

fluorescence microscopy, and analyzed using a computational workflow (see STAR Methods). The number of cells of each fluorescently labeled strain decreased linearly with each dilution, with the exception of the highest density droplets (Figure 1C), and the cell count distributions matched the expected Poisson distribution (Figure S2A). These data demonstrate at least a 64-fold linear range of the cell counting method of each fluorescent reporter. In contrast, a similar analysis using the mean fluorescence across the droplet images was inaccurate in the dilution range below 2^{-4}, which corresponds to the regime of cell counts for poorly growing strains (Figure S2B). Accurate quantification of low cell counts is important for estimating interaction strengths. In a separate experiment described below involving growth of fluorescently labeled strains in droplets (Table S1, E6), we analyzed the relationship between droplet diameter and the number of fluorescently labeled cells to determine if the experimental noise in this parameter contributed to the variability in cell growth across droplets. Our results showed that an ~8-μM variation in droplet diameter did not correlate with the number of cells labeled with CFP, YFP, or RFP, demonstrating that this factor did not substantially contribute to differences in cell counts among droplets (Figures S2C–S2E).

Investigating Microbial Interaction Networks in Two-Member Consortia

To determine whether MINI-Drop could illuminate microbial interactions in synthetic consortia, we investigated two-member consortia engineered to display defined interactions. A microbial interaction was defined as a statistically significant difference in the average number of cells of a given strain in the presence of a second strain (partner) compared to the absence of the partner at a specific time point. To investigate positive interaction networks with MINI-Drop, we constructed a consortium composed of an RFP-labeled *E. coli* methionine auxotroph (EC Met-) and a GFP-labeled *B. subtilis* tryptophan auxotroph (BS Trp-, Table S1, E1). In the absence of supplemented amino acids, the growth of *B. subtilis* requires secretion of tryptophan from *E. coli* and the growth of *E. coli* requires secretion of methionine from *B. subtilis*, which together generates a bidirectional positive interaction network (Figure 2A). The two species were mixed in equal proportions based on OD600 measurements, encapsulated into droplets such that each droplet had 1–2 cells on an average according to a Poisson distribution, and the droplets were incubated at 37°C for 18 h. The fluorescence microscopy images and cell count distributions demonstrated that single-species droplets exhibited a low number of total cells, whereas droplets containing both species exhibited significantly higher number of cells of each strain (Figures 2B and 2C). The inferred interaction network exhibited bidirectional positive interactions, mirroring the topology of the expected interaction network (Figures 2A and 2D) and demonstrating that MINI-Drop could deduce positive interactions. In addition, both strains exhibited poor growth in absence of the partner strain (denoted by the size of the node in the network). The cell counts for BS Trp- and EC Met- were positively correlated, suggesting that the correlation structure in absolute abundance could be used to identify bidirectional positive interactions (Figure S3A).

Next, we investigated whether MINI-Drop could decipher negative interactions. A synthetic community was constructed wherein a GFP-labeled *E. coli* strain (sender strain) was engineered to express LuxI, a synthetase for the quorum-sensing signal C6 acyl homoserine lactone (AHL). AHL diffuses into the RFP-labeled *E. coli* strain (receiver strain), binds and activates the receptor LuxR, which regulates the expression of the MazF toxin (Figure 2E; Table S1, E2). High expression levels of the endoribonuclease MazF inhibits cell growth by inducing mRNA decay (Venturelli et al., 2017), generating a strong negative interaction from the sender to the receiver strain. To characterize this community using MINI-Drop, the sender and receiver strains were mixed in equal proportions based on OD600, encapsulated into droplets, and incubated at 37°C for 18 h. The fluorescent microscopy images and cell count distributions showed that the number of receiver cells was significantly lower in droplets containing both the sender and receiver strains compared to the average number of receiver cells in single-strain droplets (Figures 2F and 2G). The average number of sender cells in droplets containing the sender strain alone was 16.7-fold higher than the average number of receiver cells in droplets containing only the receiver strain, presumably due to leakiness of *mazF* from the pLux promoter in the absence of AHL. The inferred interaction network exhibited a strong negative interaction from the sender to the receiver and a weak negative interaction from the receiver to the sender (Figure 2H). The node size of the receiver strain was significantly smaller than the sender strain, illustrating the substantial difference in single-strain fitness in the absence of the partner. The cell counts of the sender and receiver were negatively correlated across droplets, suggesting that the correlation structure of absolute abundance could be used to pinpoint bidirectional negative interactions (Figure S3B).

The Molecular Composition of the Environment Shapes a Microbial Interaction Network

The molecular composition of the environment influences the energetic costs and benefits of microbial interactions in microbial communities (Cao et al., 2019; Harcombe et al., 2016; Liu et al., 2017). A key challenge is understanding how microbial interaction networks are modulated by environmental parameters. To investigate this question, we constructed a three-member community consisting of two strains that interact via bidirectional positive interactions and a third strain that promotes growth of constituent members of the community but does not receive a benefit from the community. Specifically, the strains included RFP-labeled *E. coli* (EC WT), CFP-labeled *E. coli* methionine auxotroph (EC Met-), and YFP-labeled *S. typhimurium* (ST Lac*) (Figure 3A). This consortium was characterized in four conditions that varied the carbon source (lactose or glucose) and the presence or absence of supplemented methionine. In lactose minimal media, *E. coli* can consume lactose and secrete carbon byproducts that can be utilized as substrates by ST Lac* (Table S1, E3–E6) (Harcombe, 2010). In the absence of supplemented methionine, the growth of EC Met- is dependent on methionine or intermediate(s) used to produce methionine that are secreted by constituent community members.

We used MINI-Drop to infer the pairwise microbial interaction network by analyzing the number of cells of each community member in single-strain and two-member droplets. In lactose minimal media lacking supplemented methionine, the inferred

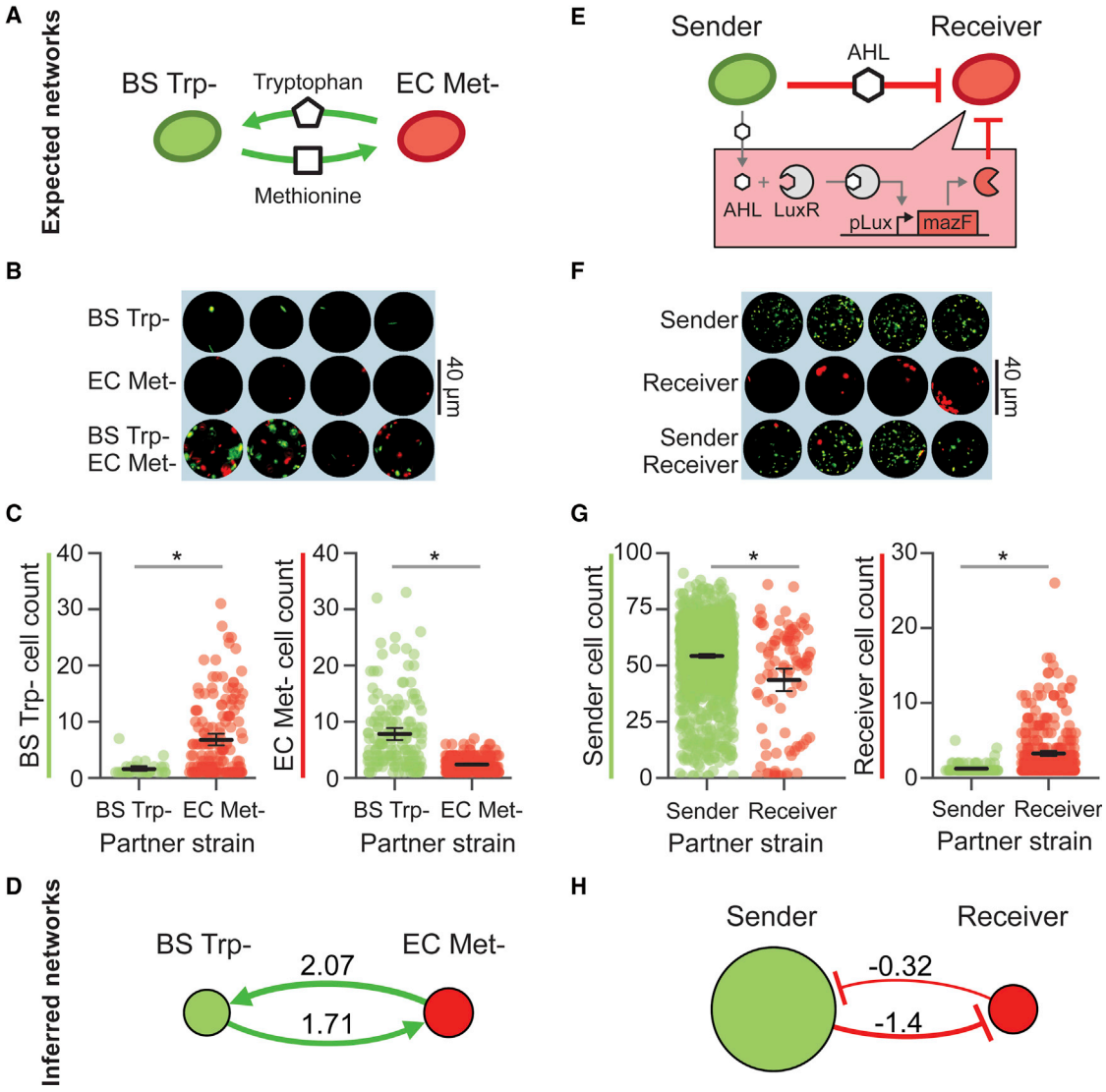

Figure 2. Investigating Positive and Negative Microbial Interaction Networks Using MINI-Drop

(A) Schematic of the expected network for a synthetic consortium composed of an RFP-labeled *E. coli* methionine auxotroph (EC Met-) and a GFP-labeled *B. subtilis* tryptophan auxotroph (BS Trp-) (Table S1, E1).

(B) Fluorescence microscopy image of representative single-species (EC Met- or BS Trp-) or two-member droplets.

(C) Categorical scatter plot showing the number of BS Trp- or EC Met- cells in each droplet. The black horizontal line represents the mean and the error bars denote bootstrapped 95% confidence intervals for the mean. Gray lines denote statistically significant difference in means based on the Mann-Whitney U test (n = 87, p = 1.5e−6, left and n =3 72, p = 3.8e−26, right).

(D) The inferred interaction network for the EC Met-, BS Trp- consortium. The edge width is proportional to the $\log_2$ ratio of the average cell count in the presence of a partner to the average cell count in single-strain droplets. Node size is proportional to the average cell count of each strain in single-strain droplets.

(E) Schematic of the expected network of an *E. coli* community that exhibits a strong unidirectional negative interaction. A GFP-labeled strain (sender) expresses LuxI, a synthetase for the quorum-sensing signal C6 acyl homoserine lactone (AHL). AHL binds to the receptor LuxR in an RFP-labeled strain (receiver) and activates the expression of a toxin MazF, generating a strong negative interaction (Table S1, E2).

(F) Fluorescence microscopy image of representative droplets containing the sender strain, receiver strain, or community.

(G) Categorical scatter plot of the number of sender or receiver cells in each droplet in the presence or absence of a partner. The black line represents the mean and the error bars denote bootstrapped 95% confidence intervals for the mean. Gray lines denote statistically significant differences in the means (n = 1512, p = 2.2e−4, left; n = 421, p = 3.8e−14, right).

(H) The inferred interaction network for the quorum sensing regulated toxin consortium.

network mirrored the expected network, exhibiting bidirectional positive interactions between ST Lac* and EC Met- and unidirectional positive interactions from EC WT to ST Lac* or to EC Met- (Figures 3A, 3E, and 3I; Table S1, E3, Table S2). In lactose minimal media supplemented with methionine, the positive outgoing interactions from EC WT or ST Lac* to EC Met- were absent in the network and bidirectional negative interactions linked EC Met- and EC WT (Figures 3B, 3F, and 3J;

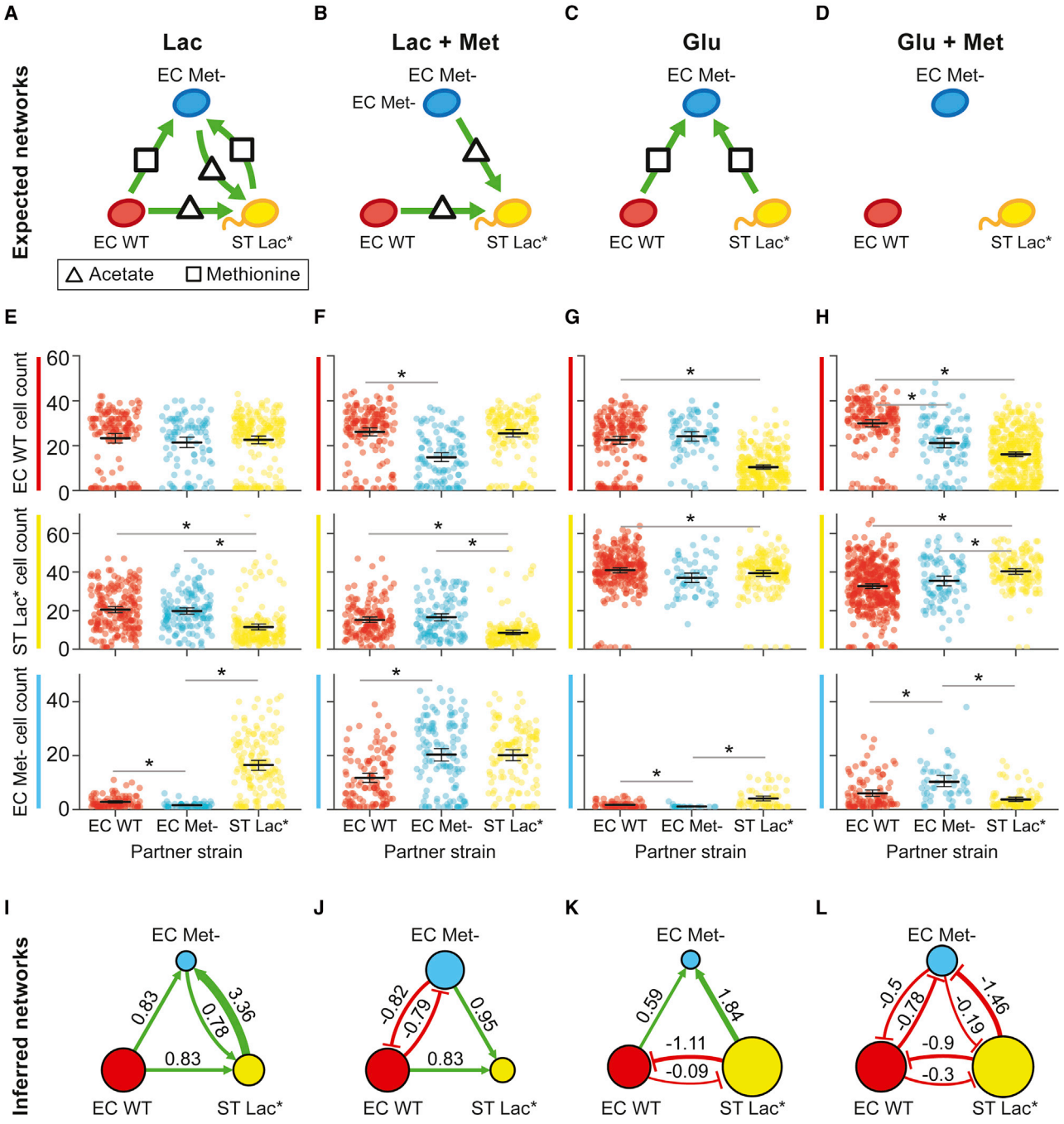

Figure 3. The Molecular Composition of the Environment Shapes the Interaction Network of a Three-Member Consortium

(A) Schematic of the expected microbial interaction network of a three-member consortium consisting of RFP-labeled *E. coli* (EC WT), CFP-labeled *E. coli* methionine auxotroph (EC Met-), and YFP-labeled *S. Typhimurium* deficient in lactose metabolism (ST Lac*) in lactose minimal media lacking supplemented methionine (Table S1, E3). Secreted carbon byproducts (acetate) and methionine are represented by a triangle and rectangle, respectively. Node colors and green arrows denote the type of fluorescent reporter and positive interactions, respectively.

(B) Schematic of the expected microbial interaction network in lactose minimal media supplemented with methionine (Table S1, E4).

(C) Schematic of the expected microbial interaction network in glucose minimal media lacking supplemented methionine (Table S1, E5).

(D) Schematic of the expected microbial interaction network in glucose minimal media supplemented with methionine (Table S1, E6).

(E) Cell count distributions in lactose minimal media for EC WT (top), ST Lac* (middle), or EC Met- (bottom). The black line represents the mean and the error bars denote the bootstrapped 95% confidence intervals for the mean. The gray horizontal bars indicate a statistically significant difference ($p < 0.05$, Table S2) based on the Mann-Whitney U test.

(F) Cell count distributions in lactose minimal media supplemented with methionine for EC WT (top), ST Lac* (middle), or EC Met- (bottom).

(G) Cell count distributions in glucose minimal media for EC WT (top), ST Lac* (middle), or EC Met- (bottom).

(legend continued on next page)

Table S1, E4). In glucose minimal media lacking supplemented methionine, the positive interactions from EC WT or EC Met- to ST Lac* were absent and instead EC WT and ST Lac* were coupled by bidirectional negative interactions (Figures 3C, 3G, and 3K; Table S1, E5). In contrast to the expected network, bidirectional negative interactions were inferred between all pairs of strains in glucose minimal media supplemented with methionine (Figures 3D, 3H, and 3L; Table S1, E6). The size of the EC WT node in the network did not vary significantly across conditions, indicating that the growth of EC WT was not sensitive to environmental changes (Figures 3I, 3J, 3K, and 3L). In contrast, the size of the EC Met- or ST Lac* nodes was larger in the presence of methionine and glucose, respectively. Across all environments, the sign of the Pearson correlation coefficient clustered according to the pairwise network topology, wherein positive or negative correlation coefficients were associated with positive or negative interactions, respectively (Figures S3 and S4). These data show that correlations in the absolute abundance of strains across droplets can be used to classify two-member network topologies.

Next, we investigated the coexistence of all three strains across environmental conditions by examining three-member droplets. The cooperative network (lactose minimal media lacking methionine) displayed the highest strain coexistence, indicating that positive interactions were critical features of the network that promoted ecological stability (Figure S5A). In contrast, the competitive network (glucose minimal media supplemented with methionine) exhibited the lowest strain coexistence across all conditions, suggesting that negative interactions can destabilize the community. Networks with combinations of positive and negative interactions displayed intermediate strain coexistence. The distributions of cell counts in three-member droplets exhibited a distinct clustering pattern in each condition, demonstrating that the environmental context is a major driver of community assembly (Figure S5B). In sum, our results demonstrate that the microbial interaction network is highly context-dependent and the network topology changes from cooperative to competitive as a function of the molecular composition of the environment.

Investigating Higher-Order Interactions Using MINI-Drop

Higher-order interactions occur when a pairwise interaction is modified in the presence of a third community member (Bairey et al., 2016; Billick and Case, 1994) and these interactions are challenging to identify in microbial communities. We defined a higher-order interaction as a difference in the presence and sign (positive or negative) of an interaction in a three-member community compared to the presence and sign of the interaction in each two-member sub-community (Figure 4A). We tested whether MINI-Drop could identify higher-order interactions by analyzing the cell count distributions of each strain in three-member droplets in addition to single-strain and two-member droplets. To do so, we studied a community consisting of RFP-labeled *E. coli* methionine auxotroph that is also deficient in lactose metabolism (EC Met- Lac*, Table S1, E7), EC Met- (CFP), and ST Lac*. In lactose minimal media lacking supplemented methionine, EC Met- and ST Lac* can secrete carbon byproducts and metabolites to rescue the methionine auxotrophy and thus together enable the growth of EC Met- Lac*. Our results showed that the number of EC Met- Lac* cells was higher in the presence of both EC Met- and ST Lac* but not in the presence of either single strain, demonstrating that MINI-Drop could identify higher-order interactions (Figure 4B, $p = 0.0012$, Table S3). In the pairwise network, EC Met- (CFP) and ST Lac* displayed bidirectional positive interactions, recapitulating the expected network topology (Figure 3A, S5C, and S5D). In addition, the cell counts of EC Met- and ST Lac* displayed a strong positive correlation consistent with a bidirectional positive interaction topology (Figure S3D).

To investigate other higher-order interactions that were present in our data, we analyzed droplets containing a three-member consortium (EC WT, EC Met-, and ST Lac), two-member sub-communities, and single strains across four different environments (Figure 3; Table S1, E3–E6). Our results illuminated a higher-order interaction in lactose minimal media (Table S1, E3, Table S3), where EC WT was significantly inhibited in the presence of both EC Met- and ST Lac*, while no negative interaction was observed in the pairwise interaction networks of EC WT co-cultured with EC Met- or ST Lac* (Figures 3A, 4D, and 4E). This higher-order interaction could be explained by enhanced growth of the mutualistic pair EC Met- and ST Lac*, which in turn negatively impacted the growth of EC WT. Higher-order interactions occurred in one of twelve possible cases (3 community members in 4 environments) in the EC Met-, EC WT, ST Lac* consortium (Table S1, E3–E6, Table S3). In sum, our results show that MINI-Drop can elucidate higher-order interactions in microbial consortia and that higher-order interactions in this consortium were infrequent across different environmental conditions.

The sensitivity of the MINI-Drop method was evaluated based on number of droplets (replicates) required to infer microbial interactions of different strengths in experiments E1–E7 (Table S1). Specifically, we analyzed the relationship between interaction strength magnitude, number of replicates, and interaction significance ($p < 0.05$) (Figure S6). Our results showed that the significance of each interaction increased exponentially as a function of the number of droplets (Figure S6A). The strength of the interaction was inversely related to the number of droplets required for statistical significance of the interaction. For example, strong interactions required as few as 15 replicates whereas weak interactions required more than 50 replicates in order to be detected (Figure S6B).

(H) Cell count distributions of EC WT (top), ST Lac* (middle), or EC Met- (bottom) in glucose minimal media supplemented with methionine.

(I) Inferred interaction network in lactose minimal media lacking supplemented methionine. The edge width is proportional to the $\log_2$ ratio of the average cell count in the presence of a partner to the average cell count in the absence of the partner. Node size is proportional to the average cell count of each strain grown in isolation.

(J) Inferred network in lactose minimal media supplemented with methionine.

(K) Inferred interaction network in glucose minimal media lacking supplemented methionine.

(L) Inferred interaction network in glucose minimal media supplemented with methionine.

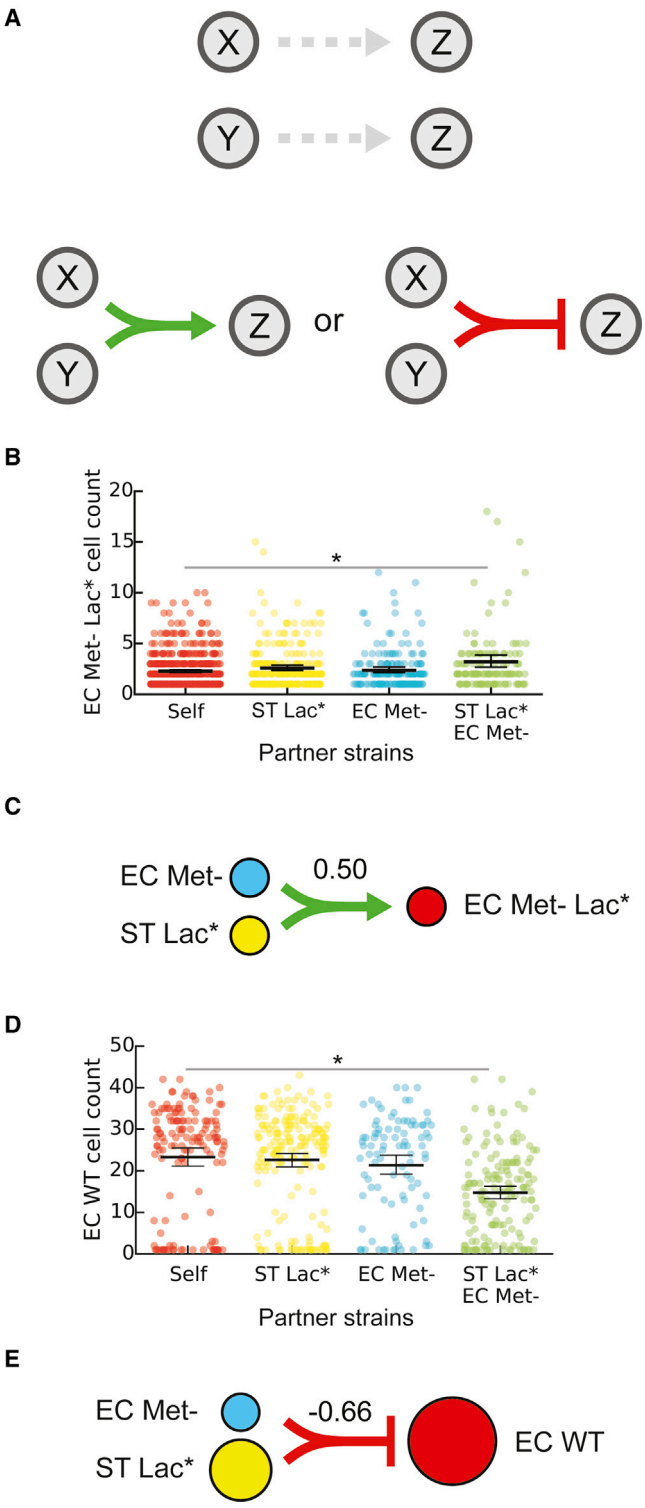

Figure 4. Investigating Higher-Order Interactions Using MINI-Drop

(A) Schematic showing an example of a higher-order interaction. Droplets containing two strains X and Z or Y and Z do not exhibit interactions. In three-member droplets, a negative or positive interaction from X and Y to Z is present and is defined as a higher-order interaction.

(B) Categorical scatter plots of the number of EC Met- Lac* cells in droplets containing the single-strain EC Met- Lac* (self), pairs of strains including EC Met- Lac* and EC Met- or ST Lac* or all three strains (EC Met- Lac*, EC Met-, and ST Lac*). Black horizontal bars denote the mean number of cells per droplet and error bars represent the bootstrapped 95% confidence interval for the mean. The horizontal bar (gray) represents a statistically significant difference in means based on the Mann-Whitney U test (p = 1.2e−3, n = 703, Table S3).

(C) Schematic showing the higher-order inferred network for the data shown in panel (B). The line width represents the inferred strength of the higher-order interaction. Node size is proportional to the average cell count of each strain grown in isolation.

(D) Categorical scatter plots of the number of EC WT cells in droplets containing the single-strain EC WT, two strains including EC WT and ST Lac* or EC Met-, or all three strains (EC WT, ST Lac*, and EC Met-) in lactose minimal media. The horizontal bar (gray) represents a statistically significant difference in means based on the Mann-Whitney U test (p = 2.9e−10, n = 296, Table S3).

(E) Schematic showing a higher-order interaction inferred using the data shown in (D). The line width represents the strength of the inferred higher-order interaction. Node size is proportional to the average cell count of each strain grown in isolation.

Discrete-Time Markov Model of Community Assembly

A stochastic population dynamic model was constructed to understand community assembly from a small number of cells and the heterogeneity in community composition across droplets. In small microbial populations, stochastic variation in intracellular molecular concentrations can impact community assembly and functions (Boedicker et al., 2009; Connell et al., 2014; Hansen et al., 2016). To model community assembly in small populations, microbial growth can be represented as a probabilistic event, such that two communities seeded with the same initial strain composition exhibit different steady-state community compositions (Figure 5A) (Horowitz et al., 2010). We investigated whether the model could be parameterized to recapitulate the cell count distributions in two and three strain droplets.

In the model, communities are seeded according to a Poisson distribution with $\lambda = 1.5$. Seeded communities that do not contain both strains were discarded and resampled. At each time step, strain *i* can undergo cell division, death, or remain static according to the probabilities $P_{div,i}$, $P_{death,i}$, and $P_{static,i}$, respectively (Figure 5B). The cell death state can also represent a non-growing or dormant state for the duration of the experiment. The probabilities $P_{div,i}$ and $P_{static,i}$ are a function of the number of cells of each strain with parameters specific to each strain and the probability $P_{death,i}$ is a fixed parameter. Negative interactions with self or non-self are represented by inverted sigmoidal logistic functions, such that the probability of cell division is inversely related to the cell number. Positive interactions are represented as sigmoidal logistic functions, such that the probability of cell division increases as a function of the number of partner cells (see STAR Methods).

We tested whether this modeling framework could recapitulate the experimental cell count distributions based on the assumption that the measurement time points represent model steady states. Models were constructed using the positive or negative interaction functions and model parameters were identified to recapitulate the cell count distributions of each strain. We constructed a model for the EC WT, ST Lac* community grown in glucose minimal media that exhibited a bidirectional negative interaction network (Figure 5C, left). Our results showed three clusters representing distinct community states exhibiting high abundance of one strain (Figure 5C, center, clusters 1 and 4),

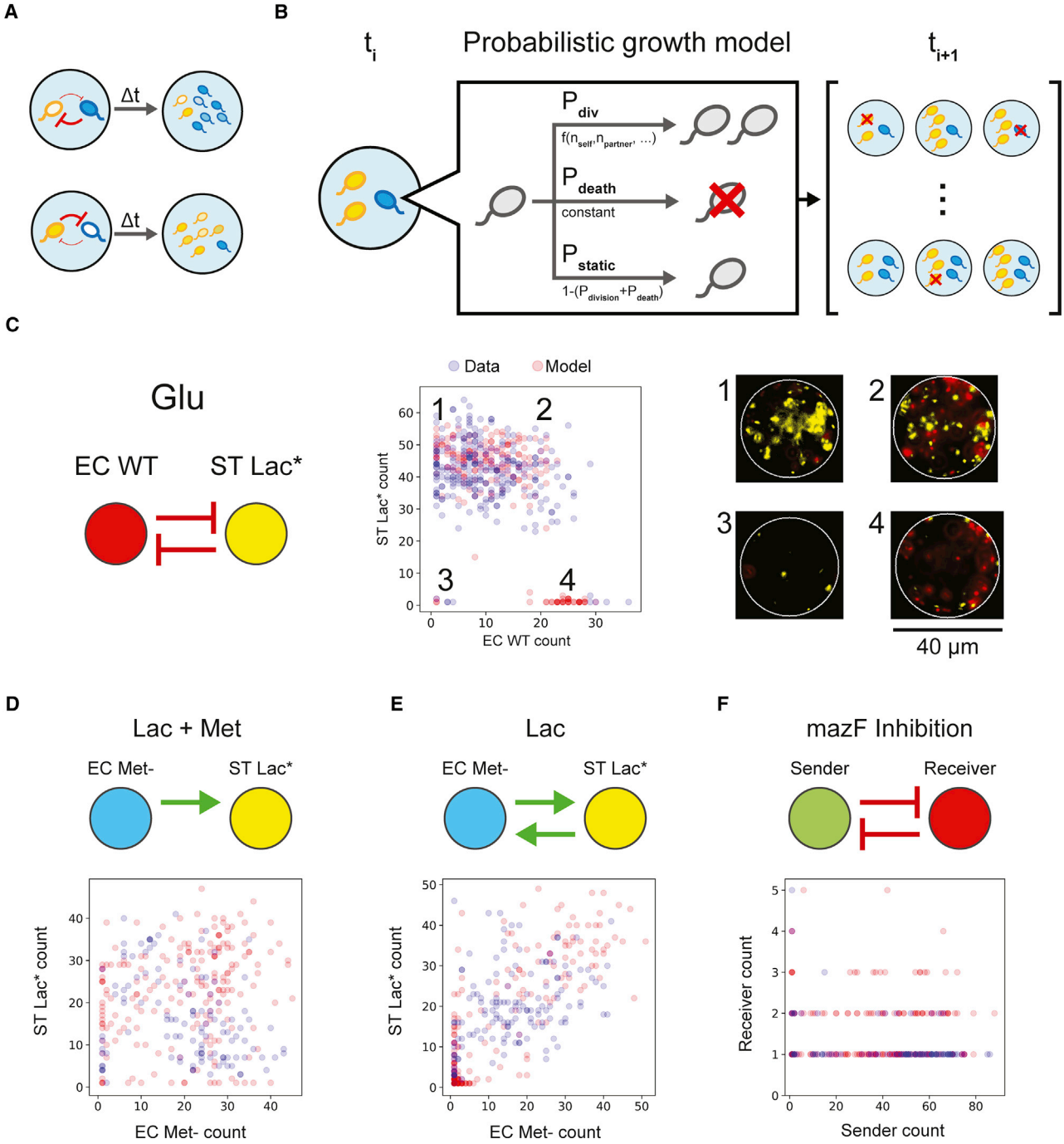

Figure 5. Discrete-Time Markov Model of Cell Growth Modified by Microbial Interactions Can Recapitulate Cell Count Distributions in Microfluidic Droplets

(A) Schematic of variability in community assembly in small populations. Stochasticity in intracellular molecular concentrations can alter the strength of microbial interactions, generating different community states (high blue cells, low yellow cells, or the reciprocal).

(B) Schematic of the discrete-time Markov model of cell growth modified by microbial interactions. At each time step, each cell can undergo cell division, cell death, or remain static according to the probabilities P_{div}, P_{death}, or P_{static}, respectively.

(C) Inferred network topology using MINI-Drop (left) for the EC WT, ST Lac* consortium in glucose minimal media (Table S1, E5). Scatter plot of experimentally measured cell counts (blue circles, n = 257) of EC WT and ST Lac* or model steady states (red circles, n = 200). This bidirectional negative interaction network generated qualitatively different community compositions corresponding to (1) low and high EC WT and ST Lac*, respectively, (2) high EC WT and ST Lac*, (3) low EC WT and ST Lac*, (4) high EC WT and low ST Lac*. Fluorescence microscopy images (right) of a representative droplet in each community state 1–4 are shown (right).

(D) Inferred network for the EC Met-, ST Lac* consortium (top) in lactose minimal media supplemented with methionine (Table S1, E4). Scatter plot of experimentally measured cell counts (blue circles, n = 118) of EC Met- and ST Lac* or model steady states (red circles, n = 200).

(legend continued on next page)

coexistence of both strains (Figure 5C, center, cluster 2), or low cell counts of both strains (Figure 5C, center, cluster 3). Representative images of droplets from each cluster showed significant differences in community composition (Figure 5C, right). A model of a bidirectional negative interaction network displaying a strong and a weak negative interaction was able to recapitulate the cell count distribution (Figure 5C, middle, Table S4).

We evaluated whether the model could recapitulate the cell count distributions of networks with positive interactions. Models constructed for the EC Met-, ST Lac* consortium in two different environments exhibiting unidirectional or bidirectional positive interactions (Table S1, E3–E4) could recapitulate the cell count distributions (Figures 5D and 5E). Next, a model was developed for the quorum sensing regulated toxin consortium (Table S1, E2) that displayed a bidirectional negative interaction network. A model of strong and weak bidirectional negative interactions recapitulated the negative correlation in the cell counts of the sender and receiver strains (Figure 5F). Our results demonstrate that bidirectional negative interaction networks can realize distinct community state distributions (Figures 5C and 5F). In the model, the number of partner cells required to impact the probability of cell division dictates the strength of an interaction (Figures 5F and S7A). The toxin mediated negative interaction in the quorum sensing regulated toxin consortium (Table S1, E2) exhibited a higher sensitivity to partner cell number than the negative interaction from ST Lac* to EC WT in glucose minimal media (Table S1, E5; Figure S7A). Therefore, the recipients of the strong negative interactions displayed different sensitivities to variations in donor cell number, providing insight into the differences in the cell count distributions.

Next, we tested whether the model could capture the experimental cell count distributions in two and three-member droplets using a single parameter set. A model parameterized to the cell count distributions of the EC WT, EC Met-, and ST Lac* consortium in glucose minimal media lacking supplemented methionine (Table S1, E5) recapitulated the experimental distributions in two and three-member droplets (Figure S8). In sum, the model was able to describe the cell count distributions for positive and negative interactions mediated by distinct molecular mechanisms, illustrating that a probabilistic growth model can explain the heterogeneity in community states in small populations.

Investigating Pairwise and Higher-Order Drug Interactions on Community Assembly

Antibiotic administration is a severe perturbation that alters community composition by reducing diversity in the human gut microbiome for a period of time before recovery (Palleja et al., 2018; Shaw et al., 2019). Synergistic or antagonistic interactions between different antibiotics can increase or reduce the effects of each single antibiotic on bacterial growth and viability. Previous work has investigated drug interactions on single bacterial strains but the effects of combinations of antibiotics on community assembly and interactions remains largely unknown (Kulesa et al., 2018; Tekin et al., 2018). Microbial interactions have been shown to be major variables shaping antibiotic tolerance in microbial communities (Adamowicz et al., 2018; Radlinski et al., 2017). We investigated whether MINI-Drop could elucidate the web of interactions linking antibiotic and species in a three-member microbial consortium consisting of EC Met-, ST Lac*, and RFP-labeled *Methylobacterium extorquens* (ME), a soil bacterium that can degrade methylamine to produce ammonia (Adamowicz et al., 2018). The effectiveness of antibiotics can vary with temperature (Cruz-Loya et al., 2019) and the growth of ME is inhibited by elevated temperatures (Attwood and Harder, 1972). Therefore, we sought to determine the effect of temperature on the interaction network.

The community was encapsulated in a modified Hypho medium (STAR Methods, Table S5) with all single and pairwise combinations of carbenicillin (CRB), streptomycin (STR), and erythromycin (ERY) at sub-lethal concentrations (Figures S9A–S9C; Table S1, E8–E21). The droplets in each condition were partitioned into two aliquots, incubated at 30°C or 37°C, and then imaged following 36 or 18 h, respectively, to account for slower growth kinetics at the lower incubation temperature (Figure 6A). We inferred the interaction networks in each condition using the same analysis methods as the experiments described above (Figures S10A and S10B). Because of the complexity of the system, we further analyzed the data to quantify various levels of interaction between combinations of antibiotics and species. Pairwise interactions between species (species-species) and each antibiotic and species (antibiotic-species) were determined by evaluating the ratio of the mean number of cells in the presence of a partner strain or antibiotic to the absence of these factors (Tables S6–S8; Figures 6B and 6C). Higher-order interactions were inferred by evaluating how antibiotic-species interactions changed in the presence of a second antibiotic or species (species-antibiotic-species or antibiotic-antibiotic-species) (Tables S6–S8; Figures 6B and 6C).

Our results showed that ST Lac* provided a substantial growth benefit to EC Met- at both temperatures, presumably due to cross-feeding of methionine or missing intermediate(s) required to produce methionine. Notably, this positive interaction was preserved in the presence of ERY, eliminated with the addition of either STR or CRB, and maintained in the presence of both ERY and CRB (Figures S10A and S10B). Weak negative interactions were present in most cases where substantial growth of both species was detected, suggesting that growth correlated activities such as microbial competition or production of toxic compounds was a prevalent mode of interaction. At 30°C, the outgoing interaction from EC Met- to ME displayed a sign change from negative to positive with the addition of STR, demonstrating that the action of STR induced a growth benefit of ME in the presence of EC Met- (Figure S10A).

For antibiotic-microbe interactions, STR primarily inhibited the growth of EC Met- without substantially suppressing the growth of ME or ST Lac* at both temperatures, mirroring the differences in susceptibility to STR in a larger population in microtiter plates (Figure S9C). ERY weakly inhibited the growth of all three strains

(E) Inferred interaction network for the EC Met-, ST Lac* consortium in lactose minimal media (top, Table S1, E3). Scatter plot of experimentally measured cell counts (blue circles, n = 141) of EC Met- and ST Lac* or model steady states (red circles, n = 200).

(F) Inferred interaction network for the sender, receiver consortium (top, Table S1, E2). Scatter plot of experimentally measured cell counts (blue circles, n = 93) of the sender and receiver strains or model steady states (red circles, n = 200).

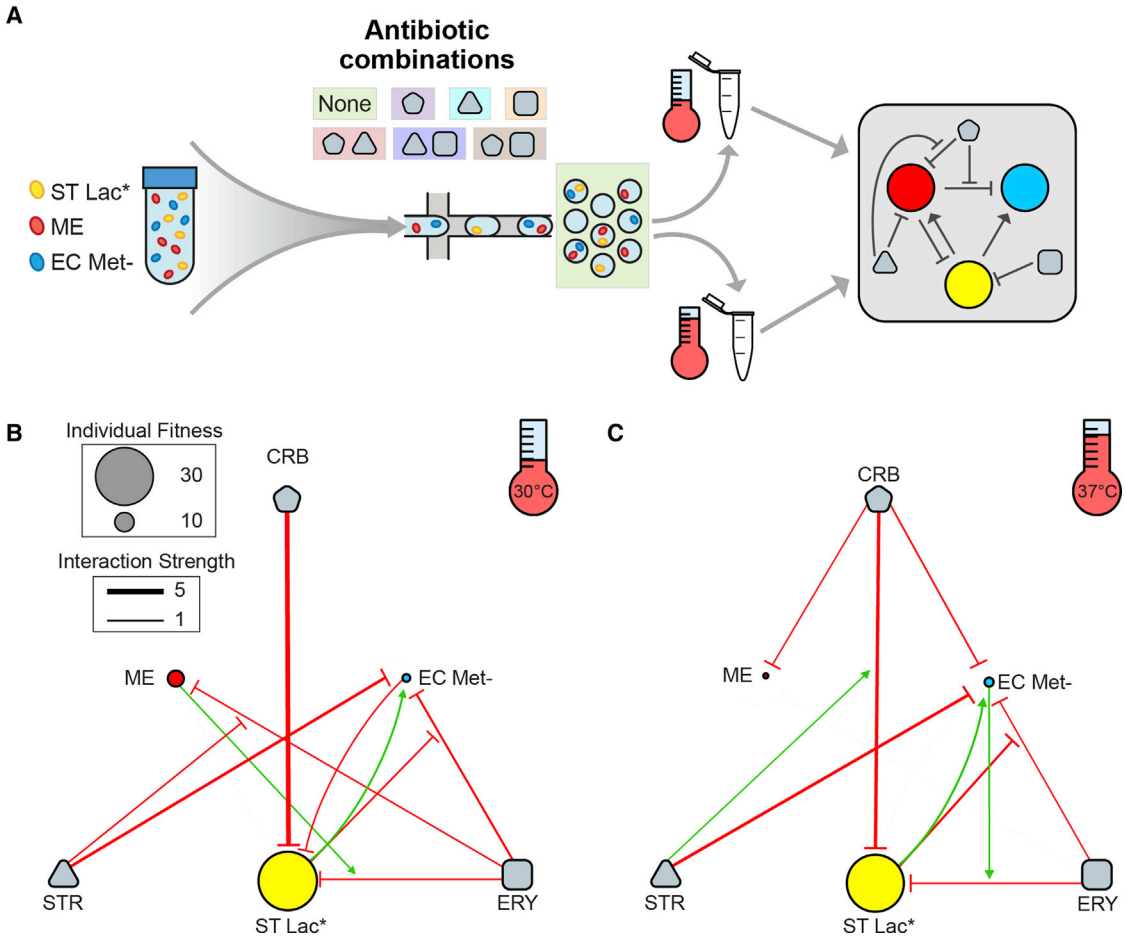

Figure 6. Combinatorial Effects of Antibiotics on Community Interactions and Assembly

(A) Overview schematic of the experimental design. A three-member community containing ST Lac*, ME, and EC Met- in modified Hypho medium was encapsulated with no antibiotics and with each individual and pairwise combination of carbenicillin (CRB), erythromycin (ERY), and streptomycin (STR). Droplets were incubated at 30°C or 37°C prior to imaging and interaction network inference.

(B) Inferred interaction network after incubation at 30°C for 36 h. The edge width is proportional to the $\log_2$ ratio of the average cell count between two conditions of interest (Tables S6–S8). Only those edges with $p < 0.05$ and $\log_2$ ratio magnitude greater than 0.5 are shown (all interactions are listed in Tables S7 and S8). Node size is proportional to the mean number of cells in single-strain droplets in the absence of antibiotics. The arrows have a sign modifier based on the level of interaction as summarized in Table S6. For example, species-antibiotic-species interactions with a value greater than 1 are visualized as an inhibitory edge pointing to an inhibitory edge, with the net result being an increase in growth of the target species. This network representation was chosen such that each edge represents the ratio between two populations of droplets differing only by the presence of one variable (i.e., species or antibiotic) and is not meant to imply mechanisms of interaction.

(C) Inferred interaction network after incubation at 37°C for 18 h.

at 30°C, consistent with the microtiter plate experiment that showed reduced growth of all species in the presence of ERY (Figure S9B). CRB strongly inhibited the growth of ST Lac* in both temperatures, but only substantially impacted the growth of EC Met- at 37°C, indicating that temperature is a major variable influencing antibiotic susceptibility across different species (Figures 6B and 6C).

Next, we examined how a second species impacted the interaction between an antibiotic and each community member (species-antibiotic-species interactions). The growth of EC Met- in the presence of ERY and ST Lac* was enhanced at both temperatures, suggesting that EC Met- was still able to benefit from the presence of ST Lac* despite inhibition of both strains by ERY (Figures 6B and 6C, S10A, and S10B). Interestingly, this positive interaction was not observed in the presence of CRB but was observed in the presence of both ERY and CRB (Figures S10A and S10B). The growth of ST Lac* in ERY was reduced in the presence of ME at 30°C or in the presence of EC Met- at 37°C, indicating that temperature is a critical parameter shaping microbial interaction networks (Figures 6B and 6C). In particular, while inhibition of ST Lac* by ME at 30°C was maintained in the presence of ERY and was not detected in the presence of CRB, inhibition was detected in the presence of both CRB and ERY.

We examined how combinations of antibiotics influence the effects of single antibiotics on the growth of each species (antibiotic-antibiotic-species interactions). STR enhanced the growth of ME in the presence of ERY compared to ERY alone at 30°C, representing an antagonistic relationship between STR and

ERY (Figure 6B). In contrast, the growth inhibition of ST Lac* was further enhanced in the presence of both STR and CRB relative to CRB alone at 37°C, demonstrating a synergistic relationship between STR and CRB (Figure 6C). Antagonism between STR and ERY and synergy between STR and ampicillin (same mechanism of action as CRB) have been previously reported for *E. coli*, but here we observe similar antibiotic-antibiotic interactions in different bacterial species (Yeh et al., 2006).

The antibiotic-species and antibiotic-antibiotic-species interactions were inferred by comparing cell counts from different populations of droplets. As such, differences in environmental conditions could alter cell morphology or fluorescence and potentially contribute to variation in cell counts. For example, the cell morphology of ST Lac* and to a lesser extent EC Met- in droplets containing CRB were altered compared to the absence of CRB, which could impact the accuracy of the cell counting method (Figure S9F) (Rolinson, 1980). Therefore, the magnitudes of these interactions should be considered as approximate. However, these data highlight a benefit of MINI-Drop, where a cell morphology change was detected in the presence of CRB that would have been overlooked by population-level measurements such as bulk fluorescence, selective plating, or sequencing-based methods.

To further understand how antibiotics impact community assembly, we evaluated the effects of antibiotics on species coexistence in three-member droplets (Figures S9D and S9E). The presence of antibiotics globally reduced coexistence relative to the no antibiotic condition. In 30°C CRB conditions, coexistence was almost entirely eliminated because of its extreme impact on the growth of ST Lac* (Figure 6B). Coexistence was lower in the presence of STR-CRB at 37°C relative to either STR or CRB alone, likely due to the synergistic impact of these antibiotics on growth inhibition of ST Lac* (Figure 6C). Additionally, higher levels of coexistence were observed in all conditions containing CRB at 37°C compared to 30°C, potentially attributed to reduced inhibition of ST Lac* by CRB at 37°C.

DISCUSSION

We showed that MINI-Drop can rapidly infer pairwise as well as higher-order microbial interactions in two and three-member consortia in different environmental conditions compared to traditional methods to study microbial interaction networks (Friedman et al., 2017; Venturelli et al., 2018). While all of the examples in this work involved bacteria expressing fluorescent proteins, orthogonal fluorescent labeling of the bacterial outer membranes and proteins via click chemistry before encapsulation in droplets could be used to apply MINI-Drop to organisms that are not genetically tractable (Geva-Zatorsky et al., 2015; Hudak et al., 2017). In addition, droplets could be injected with fluorescent stains for metabolic activity, cell damage, nucleic acid content, or reagents for biochemical assays to potentially distinguish different species and characterize single-cell phenotypes in a microbial community (Maurice and Turnbaugh, 2013). This method can be scaled to quantify interactions in higher-dimensional (>3 members) communities using compatible fluorescent labels or combinatorial fluorescent imaging of multiple reporters within the same cell. While the requirement for orthogonal fluorescent labels does limit the scalability of this approach, MINI-Drop provides the foundation for the development of imaging-independent techniques that could be applied to higher complexity communities.

In MINI-Drop, a single experiment generates hundreds to thousands of replicates of many sub-communities. The mean number of cells per drop following cell encapsulation can be manipulated to investigate the contribution of initial cell density to microbial interactions or increase the proportion of multi-strain droplets for interrogation of higher-order interactions. In the three-member consortium (Table S1, E3–E6), strains with higher fitness in the absence of a partner tended to display outgoing negative interactions, whereas strains with lower fitness had the propensity for incoming positive interactions. Therefore, the competitive ability of the strain was an indicator of outgoing negative interactions, suggesting that the unexpected negative interactions (Figure 3L) could be attributed to growth-coupled activities such as resource competition and/or metabolic waste by-product secretion. Future work could link MINI-Drop to fluorescent dye droplet barcoding to elucidate microbial interaction networks across a large number of environmental conditions in parallel (Hori et al., 2017; Kulesa et al., 2018; Miller et al., 2011). Using this droplet barcoding approach, interaction mechanisms could be inferred by screening candidate interaction-mediating molecules to identify conditions in which interactions are eliminated.

Previous methods of microbial interaction inference using modeling frameworks such as the generalized Lotka-Volterra (gLV) model are constrained by mathematical relationships (Momeni et al., 2017). For example, a gLV model of strong bidirectional positive interactions (mutualism) tends to be unstable, leading to potential underrepresentation of bidirectional positive interactions. Further, it is challenging to pinpoint if the failure of a pairwise gLV model to accurately fit experimental data is attributed to the presence of higher-order interactions or to unmodeled dynamics such as metabolites mediating the interactions. In contrast, MINI-Drop is not constrained to a defined mathematical framework and thus can readily identify higher-order interactions in the networks. We showed that MINI-Drop accurately inferred diverse interaction topologies including unidirectional positive, bidirectional positive, or bidirectional negative networks. In addition to deciphering engineered interactions, MINI-Drop illuminated pairwise interactions as well as higher-order interactions that were not designed.

The throughput of MINI-Drop was enabled by coupling two automated and scalable technologies, droplet microfluidics, and computational image analysis. The large number of sub-community replicates produced by MINI-Drop allows investigation of the contribution of initial conditions to the heterogeneity in community assembly in small populations. A probabilistic analysis of the distribution of community states provides insight into the stochastic forces shaping community behaviors. For example, we observed that bidirectional positive networks displayed frequent co-occurrence (Figures 5E, S3, and S4), whereas a bidirectional negative network can realize a set of distinct community states (Figures 5C and 5E). The correlation structure between taxa in a microbial community is frequently used to identify potential interactions based on co-occurrence or co-exclusion patterns (Faust et al., 2012). Our results suggest that correlation structure may not illuminate

negative interactions due to the potential for multiple community states. However, the mapping between correlation structure and interaction networks could differ at different population sizes and should be investigated.

Our stochastic growth model can recapitulate the heterogeneity in community states in two- and three-member consortia (Figures 5 and S8). This demonstrates that a simple probabilistic representation of cell growth, death, and microbial interactions can give rise to multiple community steady states from the same initial conditions. Our modeling framework could be used to predict the probability of strain growth as a function of the initial strain proportions and cell density. These parameters could be manipulated to maximize the likelihood of community member coexistence in multi-species consortia. Specific strains of bacteria have been shown to display positive density-dependent growth behavior referred to as an Allee effect wherein the per cell growth rate of the population is reduced in small populations (Kaul et al., 2016). We show that the model can exhibit an Allee effect and could be used to investigate key parameters influencing positive density-dependent growth behaviors in microbial populations (Figures S7B–S7D). This phenomenon is unlikely to influence the heterogeneity in community states in our experiments because of the narrow range of initial cell counts and absence of cell adhesion. The Allee effect may play a larger role in community assembly for strains that display cell adhesion since the initial number of cells in each droplet could vary over a larger range.

We used MINI-Drop to elucidate a complex network of interactions between three bacterial species exposed to different combinations of antibiotics and varying temperature. This method demonstrated that antibiotics can significantly modify the species-species interaction network and species-species interactions in turn can modulate antibiotic tolerance (Figures 6B and 6C). We identified cases of synergism and antagonism between antibiotics consistent with previous work (Yeh et al., 2006) and illuminated which combinations of antibiotic perturbations preserved or eliminated positive and negative interactions between species. In our experiments, the impact of temperature was particularly simple to assess because the population of droplets from each encapsulation could be partitioned and incubated at different temperatures. This further simplifies the application of MINI-Drop when considering environmental variables that are applied from a source external to the culture medium (e.g., gas composition, external radiation, or light). The MINI-Drop method could be used to decipher significant interactions between strains and environmental parameters, which could inform the design of interventions to steer communities to desired states.

STAR★METHODS

Detailed methods are provided in the online version of this paper and include the following:

- KEY RESOURCES TABLE
- LEAD CONTACT AND MATERIALS AVAILABILITY
  - Materials Availability Statement
- EXPERIMENTAL MODEL AND SUBJECT DETAILS
  - General Strain Maintenance: *Bacillus subtilis*, *Escherichia coli*, *Methylobacterium extorquens* AM1, and *Salmonella typhimurium* LT2
  - *Bacillus subtilis* Transformation
  - *Escherichia coli* Cloning and Transformation
- METHOD DETAILS
  - Bacterial Cell Culturing
  - Dynamic Range of Cell Counting
  - Fabrication of Microfluidic Devices
  - Encapsulation of Cells into Droplets and Fluorescence Microscopy
  - Fluorescence Microscopy Image Analysis
  - Discrete-Time Markov Model of Cell Growth
- QUANTIFICATION AND STATISTICAL ANALYSIS
- DATA AND CODE AVAILABILITY

SUPPLEMENTAL INFORMATION

Supplemental Information can be found online at https://doi.org/10.1016/j.cels.2019.06.008.

ACKNOWLEDGMENTS

We would like to thank William Harcombe (University of Minnesota) for generously providing the *E. coli* Met- (CFP), *S. Typhimurium* (YFP), and *Methylobacterium extorquens* (RFP) strains. We would like to thank Yu-Yu Cheng for assistance with construction of the engineered *B. subtilis* strain. We are grateful to Leland Hyman for assistance with droplet microfluidics and Job Grant for synthesizing surfactants for droplet microfluidics. This work was supported by the Army Research Office Young Investigator award W911NF-17-1-0296. R.L.C. was supported in part by an NHGRI training grant to the Genomic Sciences Training Program (T32 HG002760).

AUTHOR CONTRIBUTIONS

Conceptualization, O.S.V., R.H.H., R.L.C., and P.A.R.; Methodology, R.H.H. and O.S.V.; Resources, R.H.H, J.W.T., and S.G.; Investigation, R.H.H., J.W.T., R.L.C., and J.C.A.; Writing Original Draft, R.H.H., R.L.C., and O.S.V.; Writing Review & Editing: R.H.H., R.L.C., O.S.V., J.W.T., and P.A.R.; Formal Analysis, R.H.H., R.L.C., and O.S.V.; Supervision, O.S.V. and P.A.R.; funding acquisition, O.S.V.

DECLARATION OF INTERESTS

The authors declare no competing interests.

Received: January 13, 2019
Revised: April 26, 2019
Accepted: June 25, 2019
Published: September 4, 2019

REFERENCES

Adamowicz, E.M., Flynn, J., Hunter, R.C., and Harcombe, W.R. (2018). Cross-feeding modulates antibiotic tolerance in bacterial communities. ISME J. *12*, 2723–2735.

Attwood, M.M., and Harder, W. (1972). A rapid and specific enrichment procedure for Hyphomicrobium spp. Antonie Van Leeuwenhoek *38*, 369–377.

Bachmann, H., Fischlechner, M., Rabbers, I., Barfa, N., Branco dos Santos, F., Molenaar, D., and Teusink, B. (2013). Availability of public goods shapes the evolution of competing metabolic strategies. Proc. Natl. Acad. Sci. USA *110*, 14302–14307.

Bairey, E., Kelsic, E.D., and Kishony, R. (2016). High-order species interactions shape ecosystem diversity. Nat. Commun. *7*, 12285.

Berendsen, R.L., Pieterse, C.M.J., and Bakker, P.A.H.M. (2012). The rhizosphere microbiome and plant health. Trends Plant Sci. *17*, 478–486.

Billick, I., and Case, T.J. (1994). Higher order interactions in ecological communities: what are they and how can they be detected? Ecology *75*, 1529–1543.

Boedicker, J.Q., Vincent, M.E., and Ismagilov, R.F. (2009). Microfluidic confinement of single cells of bacteria in small volumes initiates high-density behavior of quorum sensing and growth and reveals its variability. Angew. Chem. Int. Ed. Engl. *48*, 5908–5911.

Cao, H.T., Gibson, T.E., Bashan, A., and Liu, Y.-Y. (2017). Inferring human microbial dynamics from temporal metagenomics data: pitfalls and lessons. BioEssays *39*, 1–12.

Cao, X., Hamilton, J.J., and Venturelli, O.S. (2019). Understanding and engineering distributed biochemical pathways in microbial communities. Biochemistry *58*, 94–107.

Clemente, J.C., Ursell, L.K., Parfrey, L.W., and Knight, R. (2012). The impact of the gut microbiota on human health: an integrative view. Cell *148*, 1258–1270.

Connell, J.L., Kim, J., Shear, J.B., Bard, A.J., and Whiteley, M. (2014). Real-time monitoring of quorum sensing in 3D-printed bacterial aggregates using scanning electrochemical microscopy. Proc. Natl. Acad. Sci. USA *111*, 18255–18260.

Cruz-Loya, M., Kang, T.M., Lozano, N.A., Watanabe, R., Tekin, E., Damoiseaux, R., Savage, V.M., and Yeh, P.J. (2019). Stressor interaction networks suggest antibiotic resistance co-opted from stress responses to temperature. ISME J. *13*, 12–23.

Dejournette, C.J., Kim, J., Medlen, H., Li, X., Vincent, L.J., and Easley, C.J. (2013). Creating biocompatible oil-water interfaces without synthesis: direct interactions between primary amines and carboxylated perfluorocarbon surfactants. Anal. Chem. *85*, 10556–10564.

Faust, K., Sathirapongsasuti, J.F., Izard, J., Segata, N., Gevers, D., Raes, J., and Huttenhower, C. (2012). Microbial co-occurrence relationships in the Human microbiome. PLoS Comput. Biol. *8*, e1002606.

Fisher, C.K., and Mehta, P. (2014). Identifying keystone species in the human gut microbiome from metagenomic timeseries using sparse linear regression. PLoS One *9*, e102451.

Friedman, J., Higgins, L.M., and Gore, J. (2017). Community structure follows simple assembly rules in microbial microcosms. Nat. Ecol. Evol. *1*, 109.

Geva-Zatorsky, N., Alvarez, D., Hudak, J.E., Reading, N.C., Erturk-Hasdemir, D., Dasgupta, S., Von Andrian, U.H., and Kasper, D.L. (2015). In vivo imaging and tracking of host-microbiota interactions via metabolic labeling of gut anaerobic bacteria. Nat. Med. *21*, 1091–1100.

Guo, M.T., Rotem, A., Heyman, J.A., and Weitz, D.A. (2012). Droplet microfluidics for high-throughput biological assays. Lab Chip *12*, 2146–2155.

Guo, X., and Boedicker, J.Q. (2016). The contribution of high-order metabolic interactions to the global activity of a four-species microbial community. PLoS Comput. Biol. *12*, e1005079.

Hansen, R.H., Timm, A.C., Timm, C.M., Bible, A.N., Morrell-Falvey, J.L., Pelletier, D.A., Simpson, M.L., Doktycz, M.J., and Retterer, S.T. (2016). Stochastic assembly of bacteria in microwell arrays reveals the importance of confinement in community development. PLoS One *11*, e0160135.

Harcombe, W. (2010). Novel cooperation experimentally evolved between species. Evolution *64*, 2166–2172.

Harcombe, W.R., Betts, A., Shapiro, J.W., and Marx, C.J. (2016). Adding biotic complexity alters the metabolic benefits of mutualism. Evolution *70*, 1871–1881.

Holtze, C., Rowat, A.C., Agresti, J.J., Hutchison, J.B., Angilè, F.E., Schmitz, C.H.J., Köster, S., Duan, H., Humphry, K.J., Scanga, R.A., et al. (2008). Biocompatible surfactants for water-in-fluorocarbon emulsions. Lab Chip *8*, 1632–1639.

Hori, Y., Kantak, C., Murray, R.M., and Abate, A.R. (2017). Cell-free extract based optimization of biomoleular circuits with droplet microfluidics. Lab Chip *17*, 3037–3042.

Horowitz, J., Normand, M.D., Corradini, M.G., and Peleg, M. (2010). Probabilistic model of microbial cell growth, division, and mortality. Appl. Environ. Microbiol. *76*, 230–242.

Hudak, J.E., Alvarez, D., Skelly, A., von Andrian, U.H., and Kasper, D.L. (2017). Illuminating vital surface molecules of symbionts in health and disease. Nat. Microbiol. *2*, 17099.

Kaul, R.B., Kramer, A.M., Dobbs, F.C., and Drake, J.M. (2016). Experimental demonstration of an Allee effect in microbial populations. Biol. Lett. *12*.

Kong, W., Meldgin, D.R., Collins, J.J., and Lu, T. (2018). Designing microbial consortia with defined social interactions. Nat. Chem. Biol. *14*, 821–829.

Kulesa, A., Kehe, J., Hurtado, J.E., Tawde, P., and Blainey, P.C. (2018). Combinatorial drug discovery in nanoliter droplets. Proc. Natl. Acad. Sci. USA *115*, 6685–6690.

Lee, T.S., Krupa, R.A., Zhang, F., Hajimorad, M., Holtz, W.J., Prasad, N., Lee, S.K., and Keasling, J.D. (2011). BglBrick vectors and datasheets: a synthetic biology platform for gene expression. J. Biol. Eng. *5*, 12.

Liu, A., Archer, A.M., Biggs, M.B., and Papin, J.A. (2017). Growth-altering microbial interactions are responsive to chemical context. PLoS One *12*, e0164919.

Loyo, C.L., and Burton, B.M. (2018). Quantitative transformation efficiency assay for Bacillus subtilis. BIO-PROTOCOL *8*, e3109.

Maurice, C.F., and Turnbaugh, P.J. (2013). Quantifying the metabolic activities of human-associated microbial communities across multiple ecological scales. FEMS Microbiol. Rev. *37*, 830–848.

Miller, O.J., El, A., Mangeat, T., Baret, J., Frenz, L., El, B., Mayot, E., Samuels, M.L., Rooney, E.K., Dieu, P., et al. (2011). High-resolution dose-response screening using droplet-based microfluidics. Proc. Natl. Acad. Sci. USA *109*, 1–6.

Momeni, B., Xie, L., and Shou, W. (2017). Lotka-Volterra pairwise modeling fails to capture diverse pairwise microbial interactions. ELife *6*, e25051.

Mounier, J., Monnet, C., Vallaeys, T., Arditi, R., Sarthou, A.S., Hélias, A., and Irlinger, F. (2008). Microbial interactions within a cheese microbial community. Appl. Environ. Microbiol. *74*, 172–181.

Palleja, A., Mikkelsen, K.H., Forslund, S.K., Kashani, A., Allin, K.H., Nielsen, T., Hansen, T.H., Liang, S., Feng, Q., Zhang, C., et al. (2018). Recovery of gut microbiota of healthy adults following antibiotic exposure. Nat. Microbiol. *3*, 1255–1265.

Park, J., Kerner, A., Burns, M.A., and Lin, X.N. (2011). Microdroplet-enabled highly parallel co-cultivation of microbial communities. PLoS One *6*, e17019.

Pulli, K., Baksheev, A., Kornyakov, K., and Eruhimov, V. (2012). Real-time computer vision with OpenCV. Commun. ACM *55*, 61–69.

Radlinski, L., Rowe, S.E., Kartchner, L.B., Maile, R., Cairns, B.A., Vitko, N.P., Gode, C.J., Lachiewicz, A.M., Wolfgang, M.C., and Conlon, B.P. (2017). Pseudomonas aeruginosa exoproducts determine antibiotic efficacy against Staphylococcus aureus. PLoS Biol. *15*, e2003981.

Rolinson, G.N. (1980). Effect of β-lactam antibiotics on bacterial cell growth rate. J. Gen. Microbiol. *120*, 317–323.

Sender, R., Fuchs, S., and Milo, R. (2016). Revised estimates for the number of human and bacteria cells in the body. PLoS Biol. *14*, e1002533.

Shannon, P., Markiel, A., Ozier, O., Baliga, N.S., Wang, J.T., Ramage, D., Amin, N., Schwikowski, B., and Ideker, T. (2003). Cytoscape: a software environment for integrated models of biomolecular interaction networks. Genome Res. *13*, 2498–2504.

Shaw, L.P., Bassam, H., Barnes, C.P., Walker, A.S., Klein, N., Balloux, F., and Shaw, L.P. (2019). Modelling microbiome recovery after antibiotics using a stability landscape framework. ISME J. *13*, 1845–1856.

Stoodley, P., Wilson, S., Hall-Stoodley, L., Boyle, J.D., Lappin-Scott, H.M., and Costerton, J.W. (2001). Growth and detachment of cell clusters from mature mixed-species biofilms. Appl. Environ. Microbiol. *67*, 5608–5613.

Tekin, E., White, C., Kang, T.M., Singh, N., Cruz-Loya, M., Damoiseaux, R., Savage, V.M., and Yeh, P.J. (2018). Prevalence and patterns of higher-order drug interactions in Escherichia coli. NPJ Syst. Biol. Appl. *4*, 31.

van der Walt, S., Colbert, S.C., and Varoquaux, G. (2011). The NumPy array: a structure for efficient numerical computation. Comput. Sci. Eng. *13*, 22–30.

Vega, N.M., and Gore, J. (2017). Stochastic assembly produces heterogeneous communities in the Caenorhabditis elegans intestine. PLoS Biol. *15*, e2000633.

Venturelli, O.S., Carr, A.C., Fisher, G., Hsu, R.H., Lau, R., Bowen, B.P., Hromada, S., Northen, T., and Arkin, A.P. (2018). Deciphering microbial interactions in synthetic human gut microbiome communities. Mol. Syst. Biol. *14*, e8157.

Venturelli, O.S., Egbert, R.G., and Arkin, A.P. (2016). Towards engineering biological systems in a broader context. J. Mol. Biol. *428*, 928–944.

Venturelli, O.S., Tei, M., Bauer, S., Chan, L.J.G., Petzold, C.J., and Arkin, A.P. (2017). Programming mRNA decay to modulate synthetic circuit resource allocation. Nat. Commun. *8*, 15128.

von Bronk, B., Schaffer, S.A., Götz, A., and Opitz, M. (2017). Effects of stochasticity and division of labor in toxin production on two-strain bacterial competition in *Escherichia coli*. PLoS Biol. *15*, e2001457.

Yeh, P., Tschumi, A.I., and Kishony, R. (2006). Functional classification of drugs by properties of their pairwise interactions. Nat. Genet. *38*, 489–494.

Zhou, J., Liu, W., Deng, Y., Jiang, Y.H., Xue, K., He, Z., Van Nostrand, J.D., Wu, L., Yang, Y., and Wang, A. (2013). Stochastic assembly leads to alternative communities with distinct functions in a bioreactor microbial community. MBio *4*, e00584–12.

STAR★METHODS

KEY RESOURCES TABLE

REAGENT or RESOURCE	SOURCE	IDENTIFIER
Bacterial and Virus Strains		
B. subtilis 168, trpC2, cat	Burton Lab (University of Wisconsin-Madison)	N/A
B. subtilis 168, trpC2, cat, amyE::Pveg-gfp-spec	this work	N/A
E. coli BW27783	CGSC	12119
E. coli MG1655z1	Elowitz Lab (Caltech)	N/A
E. coli BW25113 pheA::Kan	CGSC	10048
E. coli BW25113, metA::Kan	CGSC	10856
E. coli K12 BW25113, ΔmetB, att::pLC280 [kan P_L'-cfp oriR6K]	Harcombe Lab (University of Minnesota)	N/A
E. coli BW25113, pheA::Kan, pOSV006	This work	N/A
E. coli BW25113, metA::Kan, pOSV006	This work	N/A
E. coli BW27783, pOSV022	This work	N/A
E. coli MG1655z1, pOSV151	This work	N/A
M. extorquens AM1, DhprA::kan	Harcombe Lab (University of Minnesota)	N/A
S. typhimurium LT2, metA(P35L), metJ(16:IS10), att::pLC246 [kan P_L'-yfp oriR6K]	Harcombe Lab (University of Minnesota)	N/A
Chemicals, Peptides, and Recombinant Proteins		
Carbenicillin Disodium Salt	IBI Sicentific	IB02025
Erythtromycin	Sigma-Aldrich	E5389-5g
Streptomycin Sulfate Salt	Sigma-Aldrich	S9137-25g
Isopropyl β-D-1-thiogalactopyranoside	Sigma-Aldrich	I6758-5G
3M Novec 7500	3M	Novec 7500
Photoresist SU-8 3025	Microchem	SU-8 3025
Photoresist SU-8 developer	Microchem	SU-8
Dow Corning Sylgard 184 poly(dimethylsiloxane)	Dow Corning	Sylgard 184
Krytox 157 FSH	Zoro	G0706231
Jeffamine ED-900	Sigma-Aldrich	14527500ML-F
Aquapel	PPG Industries	8862547100
Recombinant DNA		
pOSV006 mCherry expression vector	this work	N/A
pOSV022 AHL production vector	this work	N/A
pVP038 amyE::Pveg-gfp-spec transformation vector	Burton Lab (University of Wisconsin – Madison)	N/A
pOSV151 AHL inducible mazF vector	this work	N/A
Software and Algorithms		
Anaconda (Python)	https://www.anaconda.com/	N/A
OpenCV	https://opencv.org/	N/A
Cytoscape 3.5	https://cytoscape.org/	N/A
MINI-Drop Image Analysis Scripts	this work	https://github.com/ryanusahk/MINI-Drop-Supplementary-Code
MINI-Drop Stochastic Model Scripts	this work	https://github.com/ryanusahk/MINI-Drop-Supplementary-Code
Deposited Data		
Cell Counts and Interaction Magnitudes	this work	Tables S1, S2, and S5–S8
Stochastic Model Parameters	this work	Table S3
Raw Image Files from MINIMini-Drop Experiments	this work	Mendeley Data, https://doi.org/10.17632/g5ch5r7d6m.1

LEAD CONTACT AND MATERIALS AVAILABILITY

Further information and requests for reagents should be directed to and will be fulfilled by the Lead Contact, Ophelia S. Venturelli (venturelli@wisc.edu).

Materials Availability Statement

Plasmids and strains generated in this study (Table S9) are available upon request.

EXPERIMENTAL MODEL AND SUBJECT DETAILS

General Strain Maintenance: *Bacillus subtilis*, *Escherichia coli*, *Methylobacterium extorquens* AM1, and *Salmonella typhimurium* LT2

All strains specified in Table S9 were maintained in 25% glycerol stocks prepared from cultures inoculated from single colonies and then stored at −80°C. Strains were recovered from glycerol stocks by inoculating liquid LB broth (Lennox, Sigma) or dilution streaking onto LB agar plates with appropriate antibiotics and culturing at 37°C, with the exception of *Methylobacterium extorquens*, which was streaked onto plates made with SOB Broth (Research Products International) and 15 g/L bacteriological agar (Bioworld) and cultured at 30°C. Precultures were inoculated either directly from glycerol stocks or from single colonies on dilution streaked plates.

Bacillus subtilis Transformation

B. subtilis was inoculated into 1 mL MC medium (Loyo and Burton, 2018) and incubated for 4 hours at 37°C for transformation. Plasmid DNA was first linearized by treatment with ScaI restriction enzyme (New England Biolabs). Next, 200 ng of plasmid DNA was added to 200μl cell culture and incubated for 2 hours at 37°C. Transformed cells were selected by plating on LB plates containing 100 μg ml^{1} spectinomycin (Gold Biotechnology). Plasmid pVP038 (Table S10) was transformed into *B. subtilis* 168, trpC2, cat to make *B. subtilis* 168, trpC2, cat, amyE::Pveg-gfp-spec (Table S9).

Escherichia coli Cloning and Transformation

PCR amplifications were performed using Phusion High-Fidelity DNA polymerase (New England Biolabs) and oligonucleotides for cloning were obtained from Integrated DNA Technologies. Standard cloning methods were used to construct plasmids. Plasmids were derived from a previously built construct library (Lee et al., 2011). Plasmids in Table S10 were transformed into strains as specified in Table S9.

METHOD DETAILS

Bacterial Cell Culturing

For experiments E1-7 (Table S1), strains were grown for approximately 12 hours at 37°C in LB medium, diluted 1:50 into fresh LB medium, and then grown to an OD600 of 0.31 as measured on a 1-cm spectrophotometer (NanoDrop Thermo Fisher Scientific). Next, the culture (3 mL) was centrifuged for 2 min at 3,500 x g and supernatant was removed. The cells were washed 4 by resuspending the pellet in 0.5 mL of minimal media and centrifuged as described above. In experiment E1 (Table S1), cells were cultured in M9 supplemented with glucose (1X M9 salts, 2 mM MgSO4, 100 μM CaCl2, 0.4% glucose), 1 mM isopropyl β-D-1-thiogalactopyranoside (IPTG, Sigma), and 25 μg/mL chloramphenicol (Sigma). The cell cultures containing different strains were normalized to an OD600 of 0.15 and mixed in a 1:1 ratio. In experiment E2 (Table S1), *B. subtilis* and *E. coli* were mixed in a 2:1 volumetric ratio to account for differences in the cell number to OD ratios. Cells were cultured in LB media containing 50 ng/mL anhydrotetracycline (aTc, Cayman Chemicals), 0.1% arabinose (Sigma) and 25 μg/mL chloramphenicol. In experiments E3-E7, cells were cultured in M9 media (1X M9 salts, 2 mM MgSO4, 100 μM CaCl2) with 1 mM IPTG supplemented with 0.4% glucose, 0.2% lactose, and/or 200 μM methionine as indicated.

In experiments E8-21 (Table S1), a single colony of ME, ST Lac* and EC Met- (CFP) were each inoculated into modified Hypho media (Table S5) for 48 hr at 30°C with shaking. The OD600 was measured for each culture. Cultures were centrifuged for 2 minutes at 3,500 g and resuspended in fresh modified Hypho medium to OD600 values of 0.20, 0.033, and 0.14 for ME, ST Lac* and EC Met-, respectively. These solutions were mixed in equal volume to form the community mixture. Immediately before cell encapsulation, antibiotic(s) (6 μg/mL carbenicillin disodium salt (Sigma), 10 μg/mL erythromycin (Sigma), and 2.5 μg/mL streptomycin sulfate salt (IBI Scientific)) were added to the community culture as specified and the culture was mixed by vortexing. All droplets for experiments E8-21 (Table S1) were encapsulated on the same day from the same community mixture to reduce variability across experiments.

Dynamic Range of Cell Counting

The bacterial strains EC Met- (CFP), EC WT (RFP), and ST Lac* (YFP) were grown in LB medium (with addition of 1 mM IPTG for EC WT) to early stationary phase, centrifuged at 18,000xg for 1 min, decanted, and resuspended in M9 minimal medium without glucose. Next, the cells were centrifuged at 18,000 x g for 1 min, decanted, and resuspended in a smaller volume of M9 minimal medium without glucose to concentrate the cells. The OD600 values of the concentrated EC Met-, EC WT and ST Lac* cultures were 14.4, 19.6, and 6.4, respectively. Equal volumes of each culture were combined to generate the mixed culture. The mixed culture

was serially diluted by a factor of 2 until a dilution of 2^{-7} was reached. The diluted cultures were encapsulated separately using the droplet maker device and the resulting droplets were imaged and quantified using the computational image analysis pipeline.

Fabrication of Microfluidic Devices

Photoresist masters of 25 μm layer height were fabricated by spinning a layer of photoresist SU-8 3025 (Microchem) onto a silicon wafer (University Wafer), then baked at 95°C for 10 minutes. Following baking, photoresist master was patterned by UV photolithography over a photomask (Data S1, CADArt). The master was subjected to post-exposure bake at 95°C for 4 min and developed in fresh SU-8 developer (Microchem) for 6 min prior to rinsing with isopropyl alcohol (Fischer Scientific) and baking at 150°C to remove the solvent. The microfluidic devices were fabricated by pouring poly(dimethylsiloxane) at a 11:1 polymer-to-crosslinker ratio (Dow Corning Sylgard 184) onto the master and curing at 65°C for 1 hr. The PDMS devices were excised with a scalpel and cored with a 0.75-mm biopsy core (World Precision Instruments) to create inlets and outlets. The device was then bonded to a microscope glass slide using an O_2 plasma cleaner (Harrick Plasma), and channels were treated with Aquapel (PPG Industries) to render them hydrophobic. Finally, the devices were baked at 65°C for 20 min to evaporate excess Aquapel prior to use.

Encapsulation of Cells into Droplets and Fluorescence Microscopy

To encapsulate cells into droplets, 1 mL syringes (BD Luer Lok) were fitted with 27-gauge needles and PE/2 tubing. 500 μL of the culture was loaded into a 1 mL syringe. Fluorinated oil (3M Novec 7500) was prepared with 2% ionic Krytox 157 FSH surfactant (experiments E1-E6) (Dejournette et al., 2013) or 2% of a block copolymer of Jeffamine ED-900 and Krytox 157 FSH (experiments E7-E21) (Holtze et al., 2008) loaded into a 1 mL syringe. The free end of the tubing was primed and inserted into the droplet-making device. Droplets were generated using flow rates of 600 μL h^{r-1} oil and 300 μL hr^{-1} cell culture at a 30 μm x 25 μm junction, which generated ~40μm diameter droplets at 4.8 kHz. After allowing at least 20 minutes for equilibration, droplets were collected into a 1.7 mL microfuge tube for at least 15 min and incubated as specified in each experiment. Droplets were loaded into chamber microscopy slides (Invitrogen C10228) and imaged with a 20X objective (Nikon, MRH10201) on a Ti-E Eclipse inverted microscope (Nikon). Fluorescence was imaged using the following filters (Chroma): (1) CFP: 436nm/20nm (ex), 480nm/40nm (em); (2) GFP: 470nm/40nm (ex), 525/50nm (em); (3) RFP: 560nm/40nm (ex), 630/70nm (em); and (4) YFP: 500nm/40nm (ex), 535nm/30nm (em).

Fluorescence Microscopy Image Analysis

Custom code in Python was used for automated cell counting in droplets and microbial interaction network inference. Droplets were identified from the phase-contrast images using the Hough transformation algorithm (OpenCV 3, Pulli et al., 2012). Droplets with a diameter 10% larger or smaller than 40 μm were removed from the dataset. Fluorescent cells were segmented by identifying connected regions using the SimpleBlobDetector object (OpenCV 3, Pulli et al., 2012). Droplets were binned by the presence or absence of each fluorescently labeled strain. For experiments E1-7 (Table S1), interaction strength from strain *j* to strain *i*, where droplet *d* contains d_k cells of strain *k*, was defined according to Equation 1.

$$log_2\left(\frac{mean(d_i \forall d | d_i>0, d_j>0)}{mean(d_i \forall d | d_i>0, d_j=0)}\right) \quad \text{(Equation 1)}$$

For experiments E8-21, interaction strengths were calculated as described in the text and summarized in Tables S6–S8. The impact of each species on each other species (species-species interaction) was inferred by comparing to the number of cells in single-species, no antibiotic droplets to two-species, no antibiotic droplets (6 possible interactions). The impact of each antibiotic on each species (antibiotic-species interaction) was inferred by comparing the number of cells in single-species, no antibiotic droplets to single-species, single-antibiotic droplets (9 possible interactions). The impact of each species on each antibiotic's impact on each other species (species-antibiotic-species interaction) was inferred by comparing the number of cells in single-species, single-antibiotic droplets to two-species, single-antibiotic droplets (18 possible interactions). Finally, antibiotic-antibiotic-species interactions were inferred by comparing the number of cells in single-species, single-antibiotic droplets to single-species, two-antibiotic droplets (9 possible interactions). Network schematics were drawn with Cytoscapecytoscape 3.5 (Shannon et al., 2003).

Discrete-Time Markov Model of Cell Growth

A discrete-time Markov model was developed to recapitulate the experimentally measured cell count distributions. At each time step, the propagation of each strain is determined by computing the probability of cell division $(P_{div,\ i})$, cell death, or cell growth dormancy for the duration of the experiment $(P_{death,i})$, and remaining unchanged $(P_{static,i})$ (Equations 2, 3, and 4).

$$P_{div,\ i} = r_{div,io} \times I_{ii}(n_i, s_{ii}, k_{ii}, a_{ii}) \times I_{ij}(n_j, s_{ij}, k_{ij}, a_{ij}) \quad \text{(Equation 2)}$$

$$P_{death,i} = r_{death,io} \quad \text{(Equation 3)}$$

$$P_{static,i} = 1 - (P_{div,i} + P_{death,i}) \quad \text{(Equation 4)}$$

The parameter $r_{div,io}$ is the basal probability of cell division for strain *i*. The parameter $r_{death,io}$ represents the probability of cell death of strain *i* (constant). n_i denotes the number of cells of strain *I* and s_{ij} defines whether the outgoing interaction of strain *j* (donor) to

strain i is positive $(s_{ij} = 1)$ or negative $(s_{ij} = -1)$. The parameters k_{ij} and a_{ij} define the sigmoidal interaction function I_{ij}, representing the incoming interaction for strain i produced by strain j (Equation 5).

$$I_{ij} = \begin{cases} \dfrac{(1+a_{ij})e^{k_{ij}n_j}}{1+a_{ij}e^{k_{ij}n_j}}, & \text{if } s_{ij} = +1 \\ \dfrac{(1+a_{ij})}{1+a_{ij}e^{k_{ij}n_j}}, & \text{if } s_{ij} = -1 \end{cases} \quad \text{(Equation 5)}$$

The negative interaction function approaches zero as a function of n_j whereas the positive interaction approaches $(1 + a_{ij})/a_{ij}$ as a function of n_j. The values of a_{ij} and $r_{div,i}$ are constrained such that $P_{div,\,i} \leq 1$ (Equation 6). The self-interaction function $I_{ii}(n_i, s_{ii}, k_{ii}, a_{ii})$ is less than one $(s_{ii} = -1)$ and approaches zero as a function of n_i, leading to saturation of the number of cells of strain i. The interaction function I_{ij}, is equal to 1 when $n_j = 0$, representing the absence of an interaction between strain i and j. In the absence of an interaction between strain i and j, $P_{div,\,i}$ is not dependent on strain j $(s_{ij} = -1, k_{ij} = 0, a_{ij} = 0)$. The outgoing interaction from the partner strain j, $I_{ij}(n_j, s_{ij}, k_{ij}, a_{ij})$, can be positive or negative depending on the value of the parameter s_{ij}. The parameters a_{ij} and k_{ij} determine the interaction sensitivity defined as the number of partner cells at the half-maximum of the interaction function, $\widehat{n}_j$ (Equation 6), and the rate of change of the interaction as a function of the number of partner cells (Equation 7).

$$\widehat{n}_j = \frac{1}{k_{ij}} \ln\left(\frac{1}{a_{ij}} + 2\right) \quad \text{(Equation 6)}$$

$$\left.\frac{dI_{ij}}{dn_j}\right|_{\widehat{n}_j} = \begin{cases} \dfrac{k_{ij}\left(\dfrac{1}{a_{ij}}+2\right)}{4(a_{ij}+1)}, & \text{if } s_{ij} = 1 \\ \dfrac{-k_{ij}\left(\dfrac{1}{a_{ij}}+2\right)a_{ij}}{4(a_{ij}+1)}, & \text{if } s_{ij} = -1 \end{cases} \quad \text{(Equation 7)}$$

At each time step, the state transition of a cell is independent of all other cells and the cell's prior history. The state transitions were simulated by sampling from a trinomial distribution determined by the probabilities $P_{div,\,i}$, $P_{death,i}$, and $P_{static,i}$. Communities were simulated for 100 time-steps wherein each time-step corresponded to 10.8 minutes of experimental time. Variables were constrained such that the cell populations reached a steady state within the simulation time. The initial conditions for the simulations were sampled from a Poisson distribution with λ=1.5. Communities that did not contain both strains were discarded and resampled. Model parameters are listed in Table S4.

QUANTIFICATION AND STATISTICAL ANALYSIS

All statistical analysis was performed using NumPy version 1.13.1 (van Der Walt et al., 2011, Python 2 or 3 distributed through Anaconda). Statistical significance (p value) between cell counts within droplets was computed using the two-sided Mann-Whitney U test. Error bars represent the 95% confidence interval of the mean.

DATA AND CODE AVAILABILITY

The droplet image analysis code and stochastic model are accessible on a GitHub repository at: https://github.com/ryanusahk/MINI-Drop-Supplementary-Code. The raw image files are available through Mendeley Data (https://doi.org/10.17632/g5ch5r7d6m.1).